Monolayer-gap modulated topological phases in twisted bilayer graphene

Jie Cao,[1] Fenghua Qi,[2,*] Hai Yang,[3] and Guojun Jin[3,4,†]
[1]*College of Science, Hohai University, Nanjing 210098, China*
[2]*School of Electronic Engineering, Nanjing Xiaozhuang University, Nanjing 211171, China*
[3]*School of Physical Science and Technology, Kunming University, Kunming 650214, China*
[4]*National Laboratory of Solid State Microstructures, Department of Physics, and Collaborative Innovation Center of Advanced Microstructures, Nanjing University, Nanjing 210093, China*

(Received 24 December 2019; revised manuscript received 24 February 2020; accepted 26 March 2020; published 20 April 2020)

We theoretically investigate concomitant topological properties of twisted bilayer graphene by a continuum model when gaps are opened in its two monolayers. An effective Hamiltonian is derived for the flat bands of a twisted bilayer in the vicinity of its Dirac points, then the topological characteristics of these flat bands can be identified for different valleys. Numerical calculations show that topological phases can be induced and modulated by the gaps in the two single layers. A phase diagram is obtained and is divided into three regions with the Chern number $C = 0, \pm 1$, respectively, separated by two straight lines. These observed phenomena can be well explained using simplified analytical treatments. Moreover, we can distinguish the flat bands into four topologically different states, which will bring applications into electronics and valleytronics.

DOI: 10.1103/PhysRevB.101.155419

I. INTRODUCTION

The experimental discoveries of superconductivity and strongly correlated Mott insulating state in twisted bilayer graphene [1,2] are significant achievements after much previous impressive research [3–23]. A twisted graphene bilayer (TGB) is constructed with two rotationally stacked graphene single layers, and its electronic band structure is sensitively dependent on the twist angle θ. At a series of special angles, called magic angles, the lower-energy bands around the zero Fermi energy are nearly flat with extremely narrow bandwidth due to strong interlayer coupling. When the bandwidth becomes comparable to or smaller than the interaction energy, the interaction-induced instability is expected to appear. Experiments reported that the flat-band effect is obvious after strong correlation is reached at a twisted angle larger than the magic angle when a hydrostatic pressure is applied [24]. A surge of theoretical works have been done on this subject for explaining these exotic phenomena [25–39].

At a small twist angle θ, a slight difference in the lattice orientation gives rise to a long-period moiré interference pattern, which means the number of carbon atoms in a unit cell will be very large. It is a challenging problem to strictly solve the single electron's wave equation in such a complex system. An alternative way is to calculate the band structure using a continuum model in the vicinity of the Dirac points in graphene monolayers (GMLs) [5,16]. However, the obtained continuum energy spectrum still contains a number of energy bands. A more simplified model is needed to describe the band structure at the zero Fermi energy. In fact, the nearly flat bands at the lowest energy are well separated by sizable energy gaps from other bands at the first magic angle. With the help of symmetry analysis, some previous works argued that it is possible to construct a two-band hexagonal lattice model to exclusively describe the flat bands [40–43]. Several effective real-space lattice models are widely used in calculating the pairing symmetry of superconducting phase in TGBs [25,33–36,44].

There is an important issue to be explored that if it is possible for the flat bands of a TGB to have any topological phase and phase transition. This is interesting but not very intuitive since the nearly flat bands are gapless in the well-known lattice models or continuum models. The gapless nature of the Dirac points are protected by the twofold rotation (C_2) and time-reversal ($\mathcal{T}$) symmetries. If $C_2\mathcal{T}$ is broken, then the Dirac points will become gapped. For instance, if one of the GMLs in the TGB is nearly aligned with the hexagonal boron nitride substrate, the broken C_2 symmetry will introduce a nonnegligible band gap in this layer [45,46]. It should be noted that a band gap arisen in any one of the GMLs will drastically change the energy dispersion at the hexagon corners of the moiré Brillouin zone (MBZ). In this paper, we will investigate the band dispersion and the Chern number of a TGB by introducing gaps in its two individual GMLs. One can find that a small gap at the hexagonal corners of the MBZ is opened, and the Chern number can be well defined if the Fermi energy locates inside this gap. The nonzero Chern numbers of the flat bands in the TGB are very robust. Furthermore, we can derive an effective Hamiltonian in the vicinity of the Dirac points for the flat bands. With the help of this effective Hamiltonian, the topology of the flat bands can be identified exactly as that for a GML. Generalizing the results of the GMLs, we can discuss the Chern numbers and the topological phase boundaries by modulating the gaps of the two monolayers. The numerical calculations also support the theoretical deduction. Analytical treatment shows that the

*Corresponding author: qifenghua.hi@163.com
†Corresponding author: gjin@nju.edu.cn

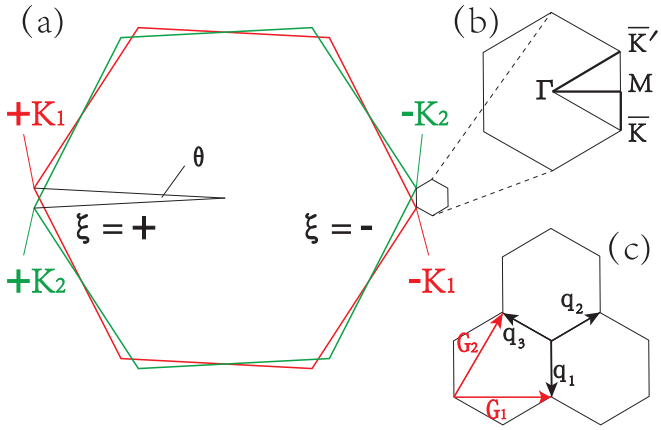

FIG. 1. (a) Schematic illustration of the Brillouin zone folding in a TGB with a small twisted angle θ. The two large hexagons represent the first Brillouin zones of the two GMLs distinguished by red (layer 1) and green (layer 2). (b) The small hexagon is the moiré Brillouin zone of the TGB. $\pm K_{1,2}$ represent the valleys in the GMLs while $\overline{K}$ and $\overline{K}'$ represent the valleys in the TGB. (c) The three $\boldsymbol{q}_n$ are the momentum transfers that correspond to the three interlayer hopping processes. $\boldsymbol{G}_i$ are the reciprocal lattice vectors.

magic angle is not influenced by the corrugation of the TGB, it is only controlled by the hopping parameter in the AB/BA stacking region which is the narrowest region in the TGB. Nevertheless, the topological property of the flat bands are strongly influenced by the corrugation tendency.

The paper is organized as follows. In Sec. II, we briefly review the effective continuum model for a TGB and calculate the low-energy spectrum in the vicinity of the Dirac points with and without the monolayer gap. In Sec. III, we discuss the topological characteristics of the flat bands from the analytical treatment. In Sec. IV, we numerically calculate the energy spectrum in the whole MBZ at the first magic angle $\theta = 1.05^\circ$ and the Chern numbers for different Fermi energies. The results show that the nonzero Chern numbers just come from the lowest-energy bands. Moreover, we discuss the topological phase transition caused by the gap difference between the two layers. A brief conclusion is presented in Sec. V.

II. EFFECTIVE CONTINUUM MODEL FOR THE TWISTED GRAPHENE BILAYER

We construct a TGB by rotating layer 1 and layer 2 with angles $-\theta/2$ and $+\theta/2$, respectively, in a totally overlapping graphene bilayer. In the momentum space, the two Dirac points from one valley are separated by $k_\theta = 2K_0 \sin(\theta/2)$, where $K_0 = 4\pi/3a$ and a is the lattice constant of each GML. After the band reconstruction, $+K_1$ and $-K_2$ are folded onto one corner ($\overline{K}'$) of the MBZ of the TGB, while $-K_1$ and $+K_2$ are folded onto the other inequivalent corner ($\overline{K}$), as shown in Fig. 1(a). When the twisted angle is small, the electronic structure can be described by a continuum model [5,16], where the intervalley mixing can be safely neglected. In a single valley, taking $\xi = +$ as an example, the low-energy band structure can be described by a Dirac model around the Dirac points of the monolayer shown in Fig. 1(b) and coupled through the moiré potential $T(\boldsymbol{r})$ [47]:

$$\mathcal{H} = \begin{pmatrix} -iv_F\boldsymbol{\sigma}_{\theta/2}\boldsymbol{\nabla} + m_1\sigma_z & T(\boldsymbol{r}) \\ T^\dagger(\boldsymbol{r}) & -iv_F\boldsymbol{\sigma}_{-\theta/2}\boldsymbol{\nabla} + m_2\sigma_z \end{pmatrix}, \quad (1)$$

where $\boldsymbol{\sigma}_{\theta/2} = e^{-(i\theta/4)\sigma_z}(\sigma_x, \sigma_y)e^{(i\theta/4)\sigma_z}$, $\boldsymbol{\nabla} = (\partial_x, \partial_y)$ and $T(\boldsymbol{r}) = \sum_{j=1}^{3} T_j e^{-i\boldsymbol{q}_j\cdot\boldsymbol{r}}$. The three-momentum transfers $\boldsymbol{q}_j$ are $\boldsymbol{q}_1 = k_\theta(0, -1)$, $\boldsymbol{q}_2 = k_\theta(\sqrt{3}/2, 1/2)$ and $\boldsymbol{q}_3 = k_\theta(-\sqrt{3}/2, 1/2)$, as shown in Fig. 1(c). According to the mass-gap correspondence in the Dirac equation [48], $m_{1(2)}$ is the GML mass term coming from the gap of layer 1(2) and it is reasonable to assume $m_{1(2)} \ll v_F k_\theta$. The symmetry of the TGB requires the interlayer coupling to have the form

$$T_j = w_{AA}\sigma_0 + w_{AB}[\sigma_x \cos(j-1)\phi + \sigma_y \sin(j-1)\phi], \quad (2)$$

where $\phi = 2\pi/3$, and w_{AA} and w_{AB} are the interlayer hopping parameters in the AA and AB stacking regions. As the first step, we assume $w_{AA} = w_{AB} = w$ and $m_1 = m_2 = m$ for simplicity. In the rest of the paper, we will focus on this valley if there is no special statement.

As the low-energy states are expected to be dominated by the individual graphene eigenstates near the original Dirac points, the dimension of Hamiltonian (1) can be cutoff to a finite value. By examining the simplest limit in which the momentum lattice is truncated at the first honeycomb shell, the Hamiltonian in the vicinity of the $\overline{K}$ point is expressed as

$$\mathcal{H}_{\boldsymbol{k}} = \begin{pmatrix} h_{\boldsymbol{k}} & T_1 & T_2 & T_3 \\ T_1^\dagger & h_{\boldsymbol{k}+\boldsymbol{q}_1} & 0 & 0 \\ T_2^\dagger & 0 & h_{\boldsymbol{k}+\boldsymbol{q}_2} & 0 \\ T_3^\dagger & 0 & 0 & h_{\boldsymbol{k}+\boldsymbol{q}_3} \end{pmatrix}, \quad (3)$$

where $\boldsymbol{k}$ is in the MBZ, $h_{\boldsymbol{k}}$ and $h_{\boldsymbol{k}+\boldsymbol{q}_j}$ are the Dirac Hamiltonians of the GML. The dependence of $h_{\boldsymbol{k}}$ and $h_{\boldsymbol{k}+\boldsymbol{q}_j}$ on the twisted angle θ is small and can be neglected. Hamiltonian (3) acts on an eight-component spinor wave function $\Psi = (\psi_0, \psi_1, \psi_2, \psi_3)^T$, where ψ_0 comes from layer 2 and ψ_1, ψ_2, ψ_3 come from layer 1. By solving the Schrödinger equation $\mathcal{H}_{\boldsymbol{k}}\Psi = E_{\boldsymbol{k}}\Psi$, we have

$$\left(E_{\boldsymbol{k}} - h_{\boldsymbol{k}} - \sum_{j=1}^{3} T_j \frac{1}{E_{\boldsymbol{k}} - h_{\boldsymbol{k}+\boldsymbol{q}_j}} T_j^\dagger\right)\psi_0 = 0. \quad (4)$$

Normally, Eq. (4) will generate eight eigenvalues of $E_{\boldsymbol{k}}$. However, at the first magic angle there exist two lowest bands well separated from other bands [1,2,42]. In the following, we intend to analytically solve Eq. (4) to obtain the effective Hamiltonian for the lowest bands.

Previous research showed that at the first magic angle of the pristine TGB there exists two lowest bands, which are degenerated at the corners of the MBZ. Therefore, in the vicinity of $\overline{K}$ and $\overline{K}'$ points, we would expect $|E_{\boldsymbol{k}}| \ll |h_{\boldsymbol{q}_j}|$ for the lowest bands. It should be stressed that we added a mass term to the GML Hamiltonian, i.e., $h_{\boldsymbol{k}} = v_F\boldsymbol{k}\cdot\boldsymbol{\sigma} + m\sigma_z$, as can be found in Eq. (1). Now for simplicity we define a bare Hamiltonian $h'_{\boldsymbol{q}} = v_F\boldsymbol{q}\cdot\boldsymbol{\sigma}$, and then $h_{\boldsymbol{k}+\boldsymbol{q}_j}$ can be expressed as $h_{\boldsymbol{k}} + h'_{\boldsymbol{q}_j}$. Because $E_{\boldsymbol{k}}$ and $h_{\boldsymbol{k}}$ are relatively small compared to $h'_{\boldsymbol{q}_j}$, $E_{\boldsymbol{k}}$ and $h_{\boldsymbol{k}}$ can be treated as the perturbation terms for the

lowest bands. Using the Dyson equation, $1/(E_{\boldsymbol{k}} - h_{\boldsymbol{k}+\boldsymbol{q}_j})$ can be expanded to the first order of $(E_{\boldsymbol{k}} - h_{\boldsymbol{k}})$ as

$$\frac{1}{E_{\boldsymbol{k}} - h_{\boldsymbol{k}} - h'_{\boldsymbol{q}_j}} = -{h'_{\boldsymbol{q}_j}}^{-1} - {h'_{\boldsymbol{q}_j}}^{-1}(E_{\boldsymbol{k}} - h_{\boldsymbol{k}}){h'_{\boldsymbol{q}_j}}^{-1}. \quad (5)$$

Using this technique, one can expand Eq. (4) to the first order of $(E_{\boldsymbol{k}} - h_{\boldsymbol{k}})$, and finally get the lowest bands equation as

$$\left[E_{\boldsymbol{k}} - h_{\boldsymbol{k}} + \sum_{j=1}^{3} T_j {h'_{\boldsymbol{q}_j}}^{-1} T_j^{\dagger} + \sum_{j=1}^{3} T_j {h'_{\boldsymbol{q}_j}}^{-1}(E_{\boldsymbol{k}} - h_{\boldsymbol{k}}){h'_{\boldsymbol{q}_j}}^{-1} T_j^{\dagger}\right]\psi_0 = 0. \quad (6)$$

After a little detailed derivation (see the Appendix), we obtain a simple expression

$$\left(E_{\boldsymbol{k}} - \frac{1-3\alpha^2}{1+6\alpha^2}h'_{\boldsymbol{k}} - \frac{1}{1+6\alpha^2}m\sigma_z\right)\psi_0 = 0, \quad (7)$$

where $\alpha = w/v_{\mathrm{F}}k_\theta$. From this equation we can see that if $\alpha^2 = 1/3$, which corresponds to the first magic angle, the effective velocity vanishes. The third term shows that the GML mass term is just modified by a factor $1/(1+6\alpha^2)$ in the TGB. If we set $m = 0$, Eq. (7) is retrieved back to

$$\left(E_{\boldsymbol{k}} - \frac{1-3\alpha^2}{1+6\alpha^2}h'_{\boldsymbol{k}}\right)\psi_0 = 0, \quad (8)$$

which is the result first obtained by Bistritzer and MacDonald [16].

It is worth mentioning that, with the same method, one can prove that the equation for the lowest two bands in the vicinity of the $\overline{K}'$ point has the same form as that for the $\overline{K}$ point.

III. ANALYTICAL RESULTS OF BERRY CURVATURE AROUND VALLEYS

Equation (7) can be seen as the effective Schrödinger equation of the lowest two bands. In other words, the effective Hamiltonian of the lowest two bands in the vicinity of the $\overline{K}$ point is

$$H_{\overline{K}} = v'_{\mathrm{F}}\boldsymbol{k}\cdot\boldsymbol{\sigma} + m'\sigma_z, \quad (9)$$

where $v'_{\mathrm{F}} = (1-3\alpha^2)/(1+6\alpha^2)v_{\mathrm{F}}$ and $m' = 1/(1+6\alpha^2)m$ are, respectively, the renormalized velocity and renormalized mass. This effective Hamiltonian is identical to the continuum model Hamiltonian of a GML with a finite mass in the vicinity of the Dirac points. Hence we can determine the topological properties of the flat bands according to the results from the individual GMLs. In each of the two GMLs, the Berry phase is mainly contributed to by the Berry curvatures concentrated in the two inequivalent valleys [49,50]. Making use of the monolayer Hamiltonian $\mathcal{H} = v_{\mathrm{F}}(\xi q_x\sigma_x + q_y\sigma_y) + m\sigma_z$, where $\xi = \pm$ for the $\pm K$ valleys, the analytical expression of the Berry curvature of the valence band in the vicinity of valleys is given as

$$\Omega(\boldsymbol{k}) = -\xi\frac{mv_{\mathrm{F}}^2}{2\left(k^2v_{\mathrm{F}}^2 + m^2\right)^{3/2}}. \quad (10)$$

As shown in Fig. 2(a), the Berry curvatures change sign for the $+K$ and $-K$ valleys, so the Chern number of the valence band $C = \frac{1}{2\pi}\int\Omega(\boldsymbol{k})d\boldsymbol{k}$ is zero as the Berry curvatures at the two valleys exactly cancel out each other. However, in the case of the TGB, the two inequivalent valleys $\overline{K}$ and $\overline{K}'$ in the MBZ come from the same valley (but different layers) of the GMLs. As shown in Fig. 2(b), the Berry curvatures have the same sign for the $\overline{K}$ and $\overline{K}'$ valleys. Hence the Chern number of the flat valence band in valley $\xi = +$ is nonzero. Furthermore, around the first magic angle, the topology of the flat bands is stable during the process of the velocity sign changing. The main reason is that the sign of any Berry curvature does not depend on the sign of the velocity according to Eq. (10), so the Chern number remains unchanged with the velocity sign changing.

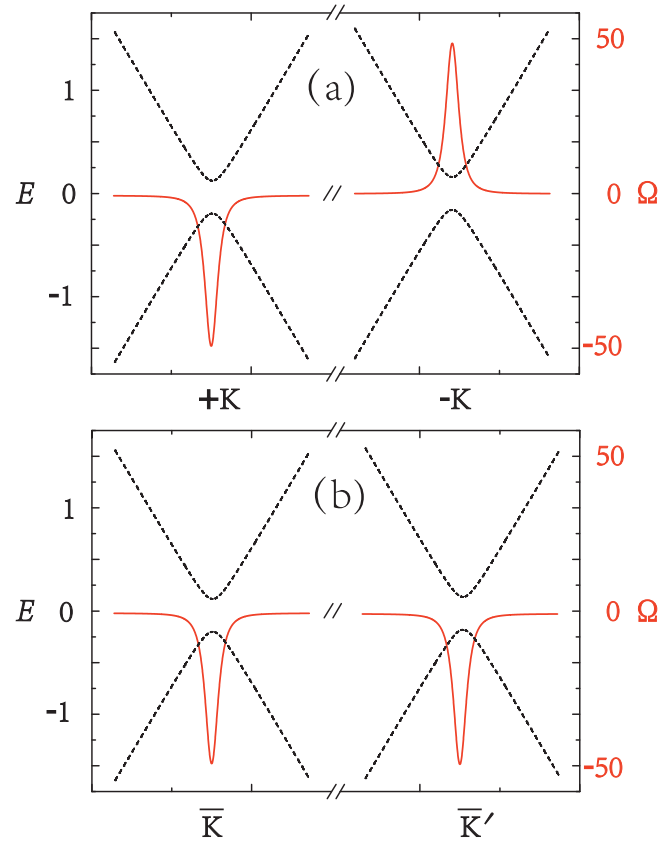

FIG. 2. Schematic illustration of the band structures (black dashed lines) and Berry curvatures (red solid lines) of a (a) GML and (b) TGB of the valence bands in the vicinity of the Dirac points. (a) In the GML, the Berry curvatures are negative in the $+K$ valley but positive in the $-K$ valley, hence the total Berry phase vanishes. (b) In the TGB, the Berry curvatures are negative for both $\overline{K}$ and $\overline{K}'$ valleys, hence the total Berry phase is nonzero. The negative values come from the fact that $\overline{K}$ and $\overline{K}'$ both come from the $\xi = +$ valley of the GMLs. For illustration only, we set $m = m' = 0.1$ and $v_{\mathrm{F}} = v'_{\mathrm{F}} = 1$.

IV. NUMERICAL RESULTS OF BAND STRUCTURES AND PHASE DIAGRAM

Unfortunately, the analytical approach cannot be generalized to the arbitrary Bloch vector $\boldsymbol{k}$ in the MBZ. It works only around the $\overline{K}$ and $\overline{K}'$ points. Away from these points, taking Γ point as an example, we can only obtain the eigenvalues from Hamiltonian (1) numerically. Notice that the moiré potential $T(\boldsymbol{r})$ hybridizes the graphene's eigenstates at $\boldsymbol{q} = \boldsymbol{k} + n_1\boldsymbol{G}_1 + n_2\boldsymbol{G}_2$, where n_1, n_2 are integers and $\boldsymbol{G}_1 = k_\theta(\sqrt{3}, 0)$, $\boldsymbol{G}_2 = k_\theta(\sqrt{3}/2, 3/2)$ are the reciprocal lattice vectors of the MBZ, as shown in Fig. 1(c). Therefore, the Hamiltonian for a single Bloch vector $\boldsymbol{k}$ in the MBZ owns the infinite dimensions. As the low-energy states are expected to be dominated by the GML eigenstates near the original Dirac points, we truncate the Hamiltonian to the finite dimensions and just keep $\boldsymbol{q}$ with $|n_1| \leqslant 4$ and $|n_2| \leqslant 4$ [42]. Then we numerically diagonalize the Hamiltonian and obtain the eigenenergies and eigenstates.

Here we take $v_F = 3at/2$, where $t = 2.6$ eV is the hopping energy between the nearest-neighbor atoms on a graphene layer. The moiré potential $T(\boldsymbol{r})$, representing the interlayer coupling, is controlled by the two parameters w_{AA} and w_{AB}, which are slightly different in the real TGB. Earlier studies assumed $w_{AA} = w_{AB}$, which corresponds to a perfectly flat TGB [20–22]. Afterwards, deepened theoretical research predicted that the optimized lattice structure of the TGB is actually corrugated in the out-of-plane direction. As a result, the interlayer spacing is the widest in the AA stacking region and the narrowest in the AB/BA stacking region. It makes w_{AA} a little smaller than w_{AB}. As shown in a numerical work [42], the difference between w_{AA} and w_{AB} makes sure that the lowest bands at the magic angle are well separated from other higher bands. In the following calculations, we take $w_{AA} = 0.08$ eV, $w_{AB} = 0.1$ eV, and $m_1 = m_2 = m$.

Figure 3 shows the band structures of the TGB at the magic angle $\theta = 1.05^\circ$ for $m = 0$ and $m = 2$ meV, respectively. In Fig. 3(a), the dispersion curves basically overlap with each other while in the enlarged plot of the zero-energy region, Fig. 3(b), the lowest flat bands indeed opens a full gap which is one order smaller than the GML mass term. Away from the $\overline{K}$ and $\overline{K}'$ points, the eigenenergy is slightly changed. The lowest bands are about 7-meV wide in the energy axis and separated from the excited bands by an energy gap about 16 meV in the upper and lower sides. If the Fermi energy lies in one of these gaps, the summation of the topological number associated with the gap can be calculated using the TKNN formula [51]

$$C = \frac{i}{A}\sum_{E_\alpha<E_F}\sum_{E_\beta>E_F}\frac{\langle\alpha|\partial\mathcal{H}/\partial k_x|\beta\rangle\langle\beta|\partial\mathcal{H}/\partial k_y|\alpha\rangle - \text{c.c.}}{(E_\alpha - E_\beta)^2}, \quad (11)$$

where A is the area of the system and $|\alpha\rangle$, $|\beta\rangle$ are the eigenstates at momenta $\boldsymbol{k}$ below and above the Fermi energy, respectively. It is worth noticing that this number is the summation of all the Chern numbers of the filling bands. In Fig. 3(a), it is shown that if the Fermi energy lies in the gaps above or below the lowest bands, we have $C = 0$. However, if the Fermi energy lies in the gap between the lowest bands, i.e, $E_F = 0$, we have $C = -1$. This

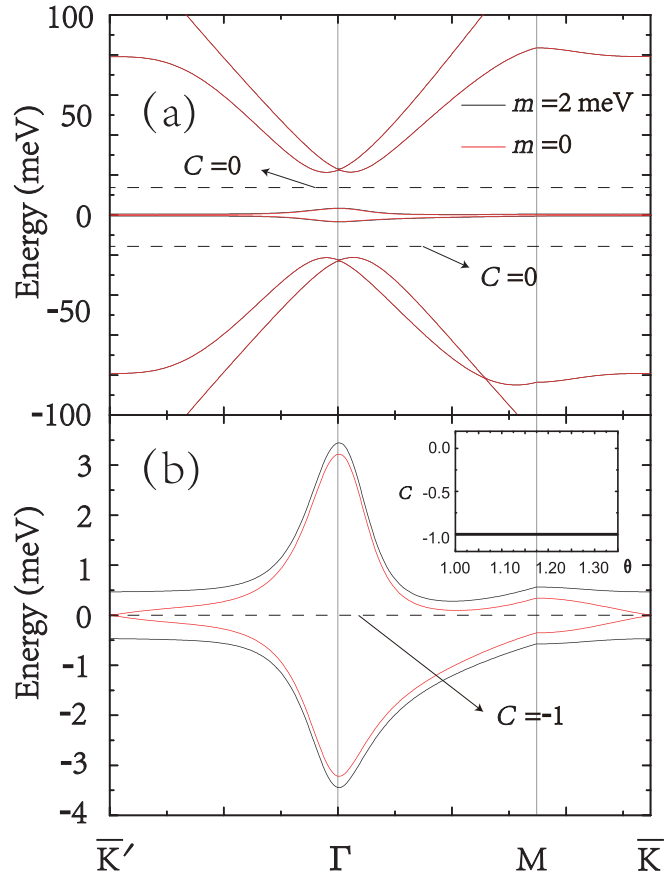

FIG. 3. (a) Energy band structure of the TGB at $\theta = 1.05^\circ$ with the GML mass term $m = 0$ (red lines) and $m = 2$ meV (black lines; actually they can be seen only in the next enlarged figure.). (b) Enlarged zero-energy region. The dashed lines represent the Fermi energy in different gaps. The total Chern number is the sum of all the Chern numbers below the Fermi energy. The inset shows that the Chern number with $E_F = 0$ does not change with twisted angles.

indicates that the nonzero Chern number just comes from the lowest bands, the valence band has the Chern number $C = -1$ and the conduction band has the Chern number $C = 1$. Furthermore, for $E_F = 0$, we calculated the Chern number with variation of the twisted angle, the results show that the Chern number does not change with the twisted angle varying from $\theta = 0.99^\circ$ to $\theta = 1.35^\circ$. The Chern number of each flat band in the TGB is very robust and no topological phase transition occurs around the first magic angle.

The numerical calculations agree well with the analytical results in Sec. III. It means that the topology is mainly controlled by the Berry curvature in the vicinity of the $\overline{K}$ and $\overline{K}'$ points. According to the Berry curvature expression in Eq. (10), the Chern number of the flat bands is only controlled by the sign of the GML mass term. If the mass term changes sign from $+1$ to -1, the Chern number of the flat valence band will change sign from -1 to $+1$. Certainly these states are both topologically nontrivial, but their chiralities are opposite. It is no doubt that this chiral difference can be verified experimentally by quantum Hall effect. The more

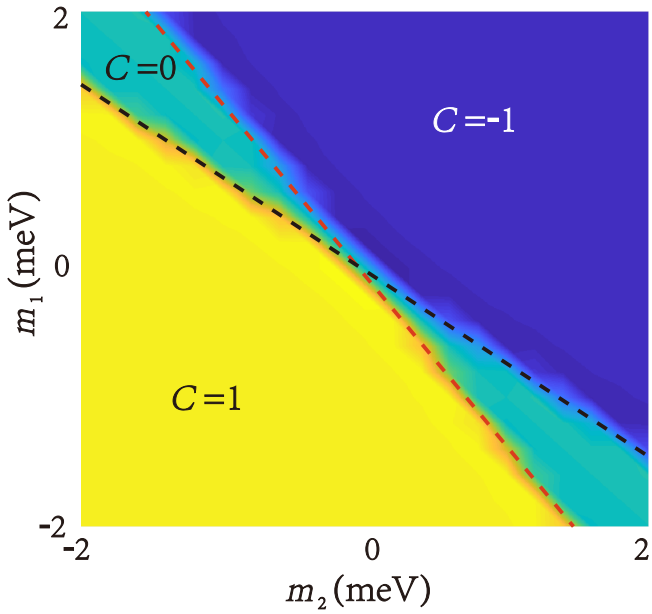

FIG. 4. Phase diagram with the variation of the mass terms, $m_{1(2)}$ for layer 1(2). The Chern number of the flat valence band can have three values, $C = 0, \pm 1$. The phase boundaries are denoted by two straight lines. The red line represents the equation $m_1 + 3(1-\beta^2)m_2 = 0$ and the black line represents the equation $m_2 + 3(1-\beta^2)m_1 = 0$. On these lines, the effective mass in the vicinity of the $\overline{K}$ or $\overline{K}'$ point is zero. Numerical fitting of these lines suggest that $\beta = 0.76$ which is very close to our parameter setting $\beta = 0.8$.

interesting case is that the mass terms in the two layers are made different from each other. This is feasible since a large number of recent researches has shown that a band gap in a GML can be produced via various ways, like substrate interactions [52,53], hydrogen adsorption [54], spin-orbit coupling [55], and uniaxial strains [56]. Would the topology of the flat bands changes from nontrivial to trivial states or vice versa? We numerically calculated this possibility where m_1 and m_2 are set as the different mass terms for layer 1 and layer 2, respectively. For instance, if we let $m_1 = -m_2$, numerical results show that the Chern number is exactly zero. This can be understood from the viewpoint of the Berry curvature in the vicinity of the $\overline{K}$ and $\overline{K}'$ points. Equation (10) shows that the sign of the Berry curvature is only determined by the sign of the effective mass at the Dirac points. If the effective masses at different valley have opposite signs, the total Berry phase cancels out for the entire MBZ.

For experimental realizations, one can introduce GML gaps in different layers via a different mechanism, such as strain engineering in one layer and substrate interaction in the other [57]. To explore the possible topological phases in the TGB by controlling the mass terms in separated layers, we investigated the phase diagram with the variation of two mass terms comprehensively. In Fig. 4 we can see that the Chern number of the flat valence band has three values, i.e, $C = -1$, $C = 0$, and $C = -1$. Like the GML, when the effective mass of one Dirac point changes sign, the topology will change from trivial to nontrivial or vice versa. Hence the phase boundary is a line where the effective mass in the vicinity of point $\overline{K}$ or $\overline{K}'$ is zero.

Let us modify Eq. (4) and solve it in the renewed situation. Due to the corrugation in the TGB, w_{AA} and w_{AB} have different values, we take $w_{\mathrm{AA}} = \beta w_{\mathrm{AB}}$ where $\beta = 0.8$ in the numerical calculations. Moreover, the two layers may have different masses, then we note $h_{\boldsymbol{k}} = h'_{\boldsymbol{k}} + m_1\sigma_z$ for layer 1 and $h_{\boldsymbol{k}+\boldsymbol{q}_j} = h'_{\boldsymbol{k}+\boldsymbol{q}_j} + m_2\sigma_z$ for layer 2. Using the Dyson equation and some simplification (see the Appendix), we have the final form in the vicinity of the $\overline{K}$ point as

$$\left[E_{\boldsymbol{k}} - \frac{1-3\alpha^2}{1+3(1+\beta^2)\alpha^2}h'_{\boldsymbol{k}} - \frac{m_1+3(1-\beta^2)m_2}{1+3(1+\beta^2)\alpha^2}\sigma_z\right]\psi_0 = 0, \tag{12}$$

where $\alpha = w_{\mathrm{AB}}/v_{\mathrm{F}}k_\theta$. Equation (12) gives us three messages. (1) The renormalized Fermi velocity can be modified by the corrugation, however, the magic angle is not influenced by the corrugation or the monolayer mass term. It is only determined by the Fermi velocity vanishing condition $1 - 3\alpha^2 = 0$, which is controlled by the interlayer hopping parameter w_{AB} in the AB/BA stacking region. (2) The phase transition induced by the monolayer mass term is also independent of the twisted angle. It is only determined by the ratio $w_{\mathrm{AA}}/w_{\mathrm{AB}}$. This means that similar topological phase transition can occur at other twisted angles. (3) The effective mass in the vicinity of the $\overline{K}$ point vanishes at $m_1 + 3(1-\beta^2)m_2 = 0$. Using the same method, one can prove that the effective mass in the vicinity of the $\overline{K}'$ point vanishes at $m_2 + 3(1-\beta^2)m_1 = 0$. These two lines in Fig. 4 define the phase boundary which perfectly matches with the numerical calculations.

V. ANALYSIS AND DISCUSSION

The stable and topologically nontrivial flat bands of the TGB near the first magic angle rely on the fact that the intervalley mixing is neglectable, then the continuum model is correct and the total Hamiltonian can be block-diagonalized into the two independent $\xi = \pm$ valleys. The $\overline{K}$ and $\overline{K}'$ valleys in the MBZ come from the same valley of the two GMLs, $+K_{1,2}$ or $-K_{1,2}$. When both of the GMLs have same topologically trivial gap, i.e., their mass terms have same sign for different valleys and layers, the Chern numbers of the flat valence band in the TGB from $\xi = +$ valley and $\xi = -$ valley have opposite signs. In this case, the TGB can be defined as a valley Chern topological insulator (VCI), because the total Chern number accounting for both valleys is zero. When only one of the GMLs has a topologically nontrivial gap, i.e., the mass term differs in the sign for different valleys, the Chern number of the flat valence band in the TGB from one valley is nonzero. In this situation, the TGB can be viewed as a Chern valley insulator (CVI), because only one valley contributes to the total Chern number. When both of the GMLs have topologically nontrivial gaps, the TGB can be either a band insulator (BI) or a Chern insulator (CI). All of the possible cases are listed in Table I. It can be expected that these states will show their different transport properties in electronics and valleytronics.

The topology of the flat bands in a TGB at the first magic angle is a cutting-edge topic. People are curious to know whether the topology of the flat bands will influence the

TABLE I. Topological states of twisted bilayer graphene with the effective masses in two single layers. For simplicity, we assume that the absolute values of the mass terms from different valleys and layers are the same. They are only different in the sign. m_i^{ξ} stands for the mass term from the valley ξ and the ith layer.

State	VCI			CVI						BI				CI	
m_1^+	+	−	+	+	−	−	+	−	+	−	+	+	−	−	+	−
m_2^+	+	−	+	+	−	−	−	+	−	+	−	−	+	+	+	−
m_1^-	+	−	+	−	+	−	+	+	−	−	+	−	+	−	−	+
m_2^-	+	−	−	+	−	+	+	+	−	−	−	+	−	+	−	+

superconducting behavior of the TGB. The very first step is to build an effective lattice model that exclusively describes the isolated flat bands near neutrality point. However, the nonzero Chern number and various symmetries together present an obstruction to construct well-localized Wannier functions [29,41–43]. This Wannier obstruction can also be understood as the lowest Landau level problem. A few works [47,58] pointed out that the wave functions of the flat bands in the TGB are reminiscent of the lowest Landau level wave functions by omitting w_{AA} term. An efficient way to overcome this obstruction is to add more bands into consideration. One can write a tight-binding model that produces multibands, and tune parameters to make two isolated bands to have the topology characteristic of the nearly flat bands of a single valley of the TGB [29,43].

It was noted that the previous research did not take into account the influence of w_{AA} term on the topological property of the lowest bands in the TGB, mainly based on two reasons. One comes from the fact that, as we derived in Eq. (12), the origin of the first magic angle is totally controlled by the strength of w_{AB}, it is legitimate to omit the w_{AA} term without changing the first magic angle. The other is that the corrugation of the TGB mainly contribute to the separation between the flat bands and the higher-energy bands, the value of w_{AA} is not interesting since its only function is to give us the correct band structure.

In our work, we argue that the w_{AA} term plays an important role in understanding the topological property of the lowest bands. In Fig. 4, we show that the topological phase boundaries are two straight lines, and the slopes of these lines are only determined by the parameter $\beta = w_{\mathrm{AA}}/w_{\mathrm{AB}}$. If m_1 and m_2 are fixed, the system can still undergos a topological phase transition via the change of β. The analytical functions of these lines $m_{1(2)} + 3(1-\beta^2)m_{2(1)} = 0$ give us two interesting scenarios: if we set $\beta = \sqrt{2/3} \approx 0.82$, then the two boundary lines will merge into one which totally annihilate the topological trivial phase ($C = 0$). In this case, any symmetry breaking term will not destroy the topological nature of the flat bands. This is unimaginable in the tight-binding model since the least we can do is to give strong lattice on-site potentials and make the system an atomic insulator (topological trivial state).

Another interesting case appears at $\beta = \sqrt{4/3} \approx 1.15$, the two boundary lines also merge into one but from the opposite direction. In this case, the topologically nontrivial phase will disappear. Recall the value $\beta \approx 0.8$ in reality [29,42], it can be confirmed that the topological nature of the flat band in the TGB comes not only from the same chirality of the Dirac nodes in each valley, but also from the corrugation tendency in real materials. If the corrugation tendency reverses (the interlayer spacing is the widest in the AB/BA stacking region and the narrowest in the AA stacking region) or strong layer coupling terms are introduced in the AA stacking region, we will get topological trivial flat bands for most of the situation.

VI. CONCLUSION

In summary, we analytically solve the band structures in the vicinity of the Dirac points in the MBZ by considering monolayer mass terms. Using the Dyson equation, we deduce an effective Hamiltonian in the vicinity of the $\overline{K}$ and $\overline{K}'$ points. We find that the effective Hamiltonian is equivalent to the continuum model Hamiltonian of the GML with a finite mass in the vicinity of the Dirac points. Hence we can treat the topology of the flat band in the TGB as same as in a GML. The topology is only determined by the sign of effective mass term in the vicinity of the $\overline{K}$ and $\overline{K}'$ points. Our analytical results show that the origin of the first magic angle is totally controlled by the strength of the w_{AB} term, while the topological property of the flat bands is relevant to the w_{AA} term.

ACKNOWLEDGMENTS

This work was supported by the Fundamental Research Funds for the Central Universities (Grant No. 2018B58714), Jiangsu Natural Science Foundation (Grant No. BK20190137), and the Yunnan Local Colleges Applied Basic Research Projects (Grant No. 2017FH001-001).

APPENDIX: SUPPLEMENTARY DERIVATION TO EQ. (12)

Let us begin from Eq. (4). Including the corrugation effect and mass difference for the two layers, Eq. (4) becomes

$$\left(E_{\boldsymbol{k}} - h_{\boldsymbol{k}}^1 - \sum_{j=1}^{3} T_j \frac{1}{E_{\boldsymbol{k}} - h_{\boldsymbol{k}+\boldsymbol{q}_j}^2} T_j^{\dagger}\right)\psi_0 = 0, \tag{A1}$$

where $h_{\boldsymbol{k}}^{1(2)} = h_{\boldsymbol{k}}' + m_{1(2)}\sigma_z$. Using the Dyson equation, $1/(E_{\boldsymbol{k}} - h_{\boldsymbol{k}+\boldsymbol{q}_j}^2)$ can be expanded to the first order of $(E_{\boldsymbol{k}} - h_{\boldsymbol{k}}' - m_2\sigma_z)$ as

$$\frac{1}{E_{\boldsymbol{k}} - h_{\boldsymbol{k}}' - m_2\sigma_z - h_{\boldsymbol{q}_j}'} = -h_{\boldsymbol{q}_j}'^{-1} - h_{\boldsymbol{q}_j}'^{-1}(E_{\boldsymbol{k}} - h_{\boldsymbol{k}}' - m_2\sigma_z)h_{\boldsymbol{q}_j}'^{-1}. \tag{A2}$$

Then Eq. (A1) can be rewritten as

$$\left[E_{\boldsymbol{k}} - h_{\boldsymbol{k}}' - m_1\sigma_z + \sum_{j=1}^{3} T_j h_{\boldsymbol{q}_j}'^{-1} T_j^{\dagger} + \sum_{j=1}^{3} T_j h_{\boldsymbol{q}_j}'^{-1}(E_{\boldsymbol{k}} - h_{\boldsymbol{k}}' - m_2\sigma_z)h_{\boldsymbol{q}_j}'^{-1} T_j^{\dagger}\right]\psi_0 = 0. \tag{A3}$$

Specifically, we have

$$T_j = w_{\mathrm{AB}}\begin{pmatrix} \beta & e^{-i\phi_j} \\ e^{i\phi_j} & \beta \end{pmatrix}, \tag{A4}$$

$$h'_{\boldsymbol{q}_j} = v_{\mathrm{F}}k_\theta\begin{pmatrix} 0 & e^{-i\phi_{\boldsymbol{q}_j}} \\ e^{i\phi_{\boldsymbol{q}_j}} & 0 \end{pmatrix}, \tag{A5}$$

and

$$h'_{\boldsymbol{k}} = v_{\mathrm{F}}\begin{pmatrix} 0 & e^{-i\phi_{\boldsymbol{k}}} \\ e^{i\phi_{\boldsymbol{k}}} & 0 \end{pmatrix}, \tag{A6}$$

where $\phi_1 = 0, \phi_2 = 2\pi/3, \phi_3 = -2\pi/3, \phi_{\boldsymbol{q}_1} = -\pi/2, \phi_{\boldsymbol{q}_2} = \pi/6, \phi_{\boldsymbol{q}_3} = 5\pi/6$, and $\beta = w_{\mathrm{AA}}/w_{\mathrm{AB}} = 0.8$ in the main text. Using the matrices (A4) to (A6), we can calculate the terms in Eq. (A3) as

$$\sum_{j=1}^{3} T_j {h'_{\boldsymbol{q}_j}}^{-1} T_j^\dagger = 0, \tag{A7}$$

$$\sum_{j=1}^{3} T_j {h'_{\boldsymbol{q}_j}}^{-1} E_{\boldsymbol{k}} {h'_{\boldsymbol{q}_j}}^{-1} T_j^\dagger = 3(1+\beta^2)\alpha^2 E_{\boldsymbol{k}}, \tag{A8}$$

$$\sum_{j=1}^{3} T_j {h'_{\boldsymbol{q}_j}}^{-1} h'_{\boldsymbol{k}} {h'_{\boldsymbol{q}_j}}^{-1} T_j^\dagger = -3\alpha^2 h'_{\boldsymbol{k}}, \tag{A9}$$

$$\sum_{j=1}^{3} T_j {h'_{\boldsymbol{q}_j}}^{-1} m_2\sigma_z {h'_{\boldsymbol{q}_j}}^{-1} T_j^\dagger = 3m_2(1-\beta^2)\sigma_z, \tag{A10}$$

where $\alpha = w_{\mathrm{AB}}/v_{\mathrm{F}}k_\theta$. Combining these equalities, Eq. (A1) is simplified to

$$\{[1+3(1+\beta^2)\alpha^2]E_{\boldsymbol{k}} - [m_1 + 3m_2(1-\beta^2)]\sigma_z - (1-3\alpha^2)h'_{\boldsymbol{k}}\}\psi_0 = 0. \tag{A11}$$

It is Eq. (12) in the main text. If we set $m_1 = m_2 = m$ and $\beta = 1$, this equation will go back to Eq. (7).

[1] Y. Cao, V. Fatemi, S. Fang, K. Watanabe, T. Taniguchi, E. Kaxiras, and P. Jarillo-Herrero, Nature **556**, 43 (2018).

[2] Y. Cao, V. Fatemi, A. Demir, S. Fang, S. L. Tomarken, J. Y. Luo, J. D. Sanchez-Yamagishi, K. Watanabe, T. Taniguchi, E. Kaxiras, R. C. Ashoori, and P. Jarillo-Herrero, Nature **556**, 80 (2018).

[3] C. Berger, Z. Song, X. Li, X. Wu, N. Brown, C. Naud, D. Mayou, T. Li, J. Hass, A. N. Marchenkov, E. H. Conrad, P. N. First, and W. A. de Heer, Science **312**, 1191 (2006).

[4] J. Hass, R. Feng, J. E. Millán-Otoya, X. Li, M. Sprinkle, P. N. First, W. A. de Heer, E. H. Conrad, and C. Berger, Phys. Rev. B **75**, 214109 (2007).

[5] J. M. B. Lopes dos Santos, N. M. R. Peres, and A. H. Castro Neto, Phys. Rev. Lett. **99**, 256802 (2007).

[6] J. Hass, F. Varchon, J. E. Millán-Otoya, M. Sprinkle, N. Sharma, W. A. de Heer, C. Berger, P. N. First, L. Magaud, and E. H. Conrad, Phys. Rev. Lett. **100**, 125504 (2008).

[7] G. Li, A. Luican, J. M. B. Lopes dos Santos, A. H. Castro Neto, A. Reina, J. Kong, and E. Y. Andrei, Nat. Phys. **6**, 109 (2010).

[8] D. L. Miller, K. D. Kubista, G. M. Rutter, M. Ruan, W. A. de Heer, P. N. First, and J. A. Stroscio, Phys. Rev. B **81**, 125427 (2010).

[9] E. J. Mele, Phys. Rev. B **81**, 161405(R) (2010).

[10] G. Trambly de Laissardière, D. Mayou, and L. Magaud, Nano Lett. **10**, 804 (2010).

[11] S. Shallcross, S. Sharma, E. Kandelaki, and O. A. Pankratov, Phys. Rev. B **81**, 165105 (2010).

[12] E. S. Morell, J. D. Correa, P. Vargas, M. Pacheco, and Z. Barticevic, Phys. Rev. B **82**, 121407(R) (2010).

[13] A. Luican, G. Li, A. Reina, J. Kong, R. R. Nair, K. S. Novoselov, A. K. Geim, and E. Y. Andrei, Phys. Rev. Lett. **106**, 126802 (2011).

[14] M. Kindermann and P. N. First, Phys. Rev. B **83**, 045425 (2011).

[15] L. Xian, S. Barraza-Lopez, and M. Y. Chou, Phys. Rev. B **84**, 075425 (2011).

[16] R. Bistritzer and A. H. MacDonald, Proc. Natl. Acad. Sci. USA **108**, 12233 (2011).

[17] J. M. B. Lopes dos Santos, N. M. R. Peres, and A. H. Castro Neto, Phys. Rev. B **86**, 155449 (2012).

[18] P. Moon and M. Koshino, Phys. Rev. B **85**, 195458 (2012).

[19] G. Trambly de Laissardière, D. Mayou, and L. Magaud, Phys. Rev. B **86**, 125413 (2012).

[20] P. Moon and M. Koshino, Phys. Rev. B **87**, 205404 (2013).

[21] M. Koshino, New J. Phys. **17**, 015014 (2015).

[22] M. Koshino and P. Moon, J. Phys. Soc. Jpn. **84**, 121001 (2015).

[23] Y. Xu and G. Jin, Europhys. Lett. **111**, 67006 (2015).

[24] M. Yankowitz, S. Chen, H. Polshyn, Y. Zhang, K. Watanabe, T. Taniguchi, D. Graf, A. F. Young, and C. R. Dean, Science **363**, 1059 (2019).

[25] C. Xu and L. Balents, Phys. Rev. Lett. **121**, 087001 (2018).

[26] L. Rademaker and P. Mellado, Phys. Rev. B **98**, 235158 (2018).

[27] J. F. Dodaro, S. A. Kivelson, Y. Schattner, X. Q. Sun, and C. Wang, Phys. Rev. B **98**, 075154 (2018).

[28] F. Wu, T. Lovorn, E. Tutuc, and A. H. MacDonald, Phys. Rev. Lett. **121**, 026402 (2018).

[29] H. C. Po, L. Zou, A. Vishwanath, and T. Senthil, Phys. Rev. X **8**, 031089 (2018).

[30] J. M. Pizarro, M. J. Calderón, and E. Bascones, J. Phys. Comm. **3**, 035024, (2019).

[31] Y.-Z. You and A. Vishwanath, npj Quantum Materials **4**, 16 (2019).

[32] X.-C. Wu, K. A. Pawlak, C.-M. Jian, and C. Xu, arXiv:1805.06906.

[33] H. Isobe, N. F. Q. Yuan, and L. Fu, Phys. Rev. X **8**, 041041 (2018).

[34] C.-C. Liu, L.-D. Zhang, W.-Q. Chen, and F. Yang, Phys. Rev. Lett. **121**, 217001 (2018).

[35] D. M. Kennes, J. Lischner, and C. Karrasch, Phys. Rev. B **98**, 241407(R) (2018).

[36] H. Guo, X. Zhu, S. Feng, and R. T. Scalettar, Phys. Rev. B **97**, 235453 (2018).

[37] V. Yu. Irkhin and Yu. N. Skryabin, JETP Lett. **107**, 651 (2018).
[38] Y.-H. Zhang, D. Mao, Y. Cao, P. Jarillo-Herrero, and T. Senthil, Phys. Rev. B **99**, 075127 (2019).
[39] B. Lian, Z. Wang, and B. A. Bernevig, Phys. Rev. Lett. **122**, 257002 (2019).
[40] N. F. Q. Yuan and L. Fu, Phys. Rev. B **98**, 045103 (2018).
[41] J. Kang and O. Vafek, Phys. Rev. X **8**, 031088 (2018).
[42] M. Koshino, N. F. Q. Yuan, T. Koretsune, M. Ochi, K. Kuroki, and L. Fu, Phys. Rev. X **8**, 031087 (2018).
[43] L. Zou, H. C. Po, A. Vishwanath, and T. Senthil, Phys. Rev. B **98**, 085435 (2018).
[44] Q.-K Tang, L. Yang, D. Wang, F.-C. Zhang, and Q.-H. Wang, Phys. Rev. B **99**, 094521 (2019).
[45] A. L. Sharpe, E. J. Fox, A. W. Barnard, J. Finney, K. Watanabe, T. Taniguchi, M. A. Kastner, and D. Goldhaber-Gordon, Science **365**, 605 (2019).
[46] Y.-H. Zhang, D. Mao, and T. Senthil, Phys. Rev. Research **1**, 033126 (2019).
[47] G. Tarnopolsky, A. J. Kruchkov, and A. Vishwanath, Phys. Rev. Lett. **122**, 106405 (2019).
[48] C. Chamon, C.-Y Hou, C. Mudry, S. Ryu, and L. Santos, Phys. Scr. **T146**, 014013 (2012).
[49] D. Xiao, W. Yao, and Q. Niu, Phys. Rev. Lett. **99**, 236809 (2007).
[50] X. Zhai and G. Jin, Phys. Rev. B **89**, 235416 (2014).
[51] D. J. Thouless, M. Kohmoto, M. P. Nightingale, and M. den Nijs, Phys. Rev. Lett. **49**, 405 (1982).
[52] S. Y. Zhou, G.-H. Gweon, A. V. Fedorov, P. N. First, W. A. de Heer, D.-H. Lee, F. Guinea, A. H. Castro Neto, and A. Lanzara, Nat. Mater. **6**, 770 (2007).
[53] M. S. Nevius, M. Conrad, F. Wang, A. Celis, M. N. Nair, A. Taleb-Ibrahimi, A. Tejeda, and E. H. Conrad, Phys. Rev. Lett. **115**, 136802 (2015).
[54] R. Balog, B. Jørgensen, L. Nilsson, M. Andersen, E. Rienks, M. Bianchi, M. Fanetti, E. Lægsgaard, A. Baraldi, S. Lizzit, Z. Sljivancanin, F. Besenbacher, B. Hammer, T. G. Pedersen, P. Hofmann, and L. Hornekær, Nat. Mater. **9**, 315 (2010).
[55] I. I. Klimovskikh, M. M. Otrokov, V. Yu. Voroshnin, D. Sostina, L. Petaccia, G. Di Santo, S. Thakur, E. V. Chulkov, and A. M. Shikin, ACS Nano **11**, 368 (2017).
[56] I. Yu. Sahalianov, T. M. Radchenko, V. A. Tatarenko, G. Cuniberti, and Y. I. Prylutskyy, J. Appl. Phys. **126**, 054302 (2019).
[57] L. Huder, A. Artaud, T. Le Quang, G. T. de Laissardière, A. G. M. Jansen, G. Lapertot, C. Chapelier, and V. T. Renard, Phys. Rev. Lett. **120**, 156405 (2018).
[58] J. Liu, J. Liu, and X. Dai, Phys. Rev. B **99**, 155415 (2019).